SUMMARY OF A STUDY TO DETERMINE LOW–VELOCITY IMPACT DAMAGE AND RESIDUAL TENSION STRENGTH FOR A THICK GRAPHITE/EPOXY MOTOR CASE

C. C. Poe, Jr.
NASA Langley Research Center
Hampton, Virginia 23665

Abstract

Impacters of various shapes and masses were dropped from various heights onto 36–mm– (1.4–in.) thick graphite/epoxy cylinders. The cylinders, which were wet–wound using graphite fibers and an epoxy resin, represented filament–wound cases (FWC) made for the booster motors of the Space Shuttle. Some of the cylinders were filled with inert propellant. Three indenters (tups) were used for the impact tests: a sharp corner and two hemispheres, one hemisphere with a 12.7–mm (0.5–in.) diameter and one with a 25.4–mm (1.0–in.) diameter. Drop height was varied, and, for the 25.4–mm (1.0–in.) diameter hemisphere, mass was also varied. The cylinders were impacted numerous times around the circumference and then cut into 51–mm– (2–in.) wide tension specimens, each containing an impact site. Because no cylinders remained, impacts with a 6.3–mm– (0.25–in.) diameter rod were simulated by quasi–statically pressing the rod against the face of surplus specimens that had been earlier cut from an empty cylinder. The size of the damage and the residual tension strength were measured. For the hemispheres, the damage initiated beneath the surface at a critical contact pressure and was not visible on the surface until an even larger pressure was exceeded. Specimens were destructively examined revealing that the damage consisted of matrix cracking and broken fibers. For the hemispherers, the tension strength was reduced considerably before the damage was visible on the surface, 30% for the 25.4–mm– (1.0–in.) diameter hemisphere and 10% for the 12.7–mm (0.5–in.) diameter hemisphere. Analytical methods were used to predict the damage and residual tension strength. A factor of safety to account for nonvisible damage was determined. This paper is a summary of that work.

Nomenclature

a	depth of impact damage below surface or depth of equivalent surface crack, m (in.)
A_{11}, A_{22}, A_{12}	constants in Hertz's equation, Pa (psi)
c	half-length of impact damage in laminate plane or half-length of equivalent surface crack, m (in.)
E_1	Young's modulus of isotropic sphere, Pa (psi)
E_{22}	Young's modulus of laminae normal to fiber direction, Pa (psi)
E_x, E_y, E_z	Young's moduli of FWC laminate, Pa (psi)
E_r, E_z	Young's moduli of transversely isotropic body, Pa (psi)
$f(\frac{a}{t}, \frac{a}{c}, \frac{c}{W}, \phi)$	correction factor to stress intensity factor for finite width and thickness
F	impact (contact) force, N (lbf)
F_{max}	maximum impact force, N (lbf)
F_{tu}	undamaged tension strength, MPa (psi)
G_{12}	shear modulus of laminae, Pa (psi)
G_{xy}, G_{zx}	shear moduli of FWC laminate, Pa (psi)
G_{zr}	shear modulus of transversely isotropic body, Pa (psi)
h	thickness, m (in.)
k_b	spring constant for beam deflection, N/m (lbf/in.)
k_1, k_2	constants in Hertz's equation, Pa (psi)
K_q	critical stress intensity factor or fracture toughness, $Pa\sqrt{mm}$, $(psi\sqrt{in.})$
KE_{eff}	effective kinetic energy, $\frac{1}{2} M v_1^2$, J (ft-lbf)
m_1, m_2	mass of impacter and composite ring, including solid propellent, kg (lbm)
M	effective mass, kg (lbm)
n_o	factor in the Hertz law, Pa (psi)
p(r)	contact pressure, Pa (psi)
p_c	average contact pressure, Pa (psi)
Q	shape factor for an elliptical crack
r_c	contact radius, m (in.)
R_i	radius of impacter, m (in.)
S_{xf}	gross laminate stress in hoop direction for failure of first ligament, Pa (ksi)
u	relative displacement between impacter and composite ring, m (in.)
u_i	local displacement (indentation) of composite ring given by Hertz's equation, m (in.)
u_b	beam type displacement (global) of composite ring, m (in.)
v_1	velocity of impacter, m/sec (in./sec)
W	width of specimen in test section, m (in.)
ν	Poisson's ratio for an isotropic material
ν_{12}	principal Poisson's ratio of laminae
ν_{xy}, ν_{yx}, ν_{xz}, ν_{yz}	Poisson's ratios of FWC laminate
ν_r, ν_{rz}	Poisson's ratios of transversely isotropic body
ν_1	Poisson's ratio of isotropic sphere
σ_{cu}	compression strength, Pa (psi)
τ_u	shear strength, Pa (psi)
ϕ	parametric angle of ellipse

Subscripts:

1, 2	principal coordinates of laminae (The 1-direction is the fiber direction.)
x, y	Cartesian coordinates (The x-direction is the axial direction of the cylinder or hoop direction of the FWC laminate.)
r, θ, z	cylindrical coordinates (The z-direction is normal to the laminate.)

Introduction

Prior to the loss of the Space Shuttle Challenger, NASA initiated a program to develop and build several sets of booster motors with graphite/epoxy cases to be used in lieu of existing motors with steel cases. These light–weight motor's were to have been used for certain Air Force missions from a new launch facility being constructed at Vandenburg Air Force Base. However, construction of the new launch facility was canceled, causing NASA to cancel the program to build the new motors. Nevertheless, research on damage tolerance yielded generic information for other applications of thick composites to motor cases and other structures. The primary contractor was Morton Thiokol Inc. The graphite/epoxy cases were made by Hercules using a wet filament–winding process, hence the name filament–wound case (FWC). It was desired, but not required, that the FWC's be reusable like the steel cases. Each light–weight motor consisted of four FWC's, a forward case, two center cases, and an aft case. The FWC's were 3.66 m (12 ft) in

diameter and were joined together with steel pins. The forward and center FWC's were 7.6 m (25 ft) in length, and the aft FWC was somewhat shorter. The thickness of the membrane region away from the ends was approximately 36 mm (1.4 in.). The ends were thicker to withstand the concentrated pin loads. The FWC's were designed primarily for internal pressure caused by the burning propellant.

The burst pressure of graphite/epoxy pressure vessels with thin walls has been shown to be reduced significantly by low—velocity impacts[1]. However, it was not known if low—velocity impacts could seriously reduce the burst pressure of pressure vessels with thick walls such as the FWC's. Therefore, an investigation was made to determine damage and reduction in tension strength caused by low—velocity impacts. It was not economically feasible to pressure test actual FWC's for the number of parameters to be studied. Thus, a 36—mm— (1.4—in.) thick cylinder was made to represent a FWC. The cylinder was 2.13 m (84 in.) long and 76.2 cm (30 in.) in diameter. The hoop and helical fiber directions of the cylinder were rotated 90° relative to those of the FWC to provide straight specimens for uniaxial tension loading in the hoop direction, the most highly stressed direction. Otherwise, uniaxial load could not be applied in the hoop direction without causing bending of the laminate, which would be unrepresentative of a FWC with internal pressure. Thus, the hoop layers of the FWC's became longitudinal layers in the cylinder. (In this paper, all references to hoop direction are to the long direction of the cylinder.) The helical layers of the cylinder were wet wound, but the longitudinal layers could not be wound on the equipment available and had to be laid by hand using unidirectional prepreg tape. Following ultrasonic inspection, the cylinder was cut into seven rings (short cylinders) that were 30.5—cm (12—in.) long.

It was originally believed that the solid propellent could be simulated in impact tests by cutting the rings into 51—mm— (2.0—in.) wide by 30.5—cm— (12—in.) long tension specimens, placing a specimen on a large block of inert solid propellent, and then dropping an impacter onto the specimen[2,3]. However, preliminary tests revealed that the solid propellent acted as a cushion reducing the impact force rather than as a mass increasing the inertia. For this reason, it was decided to drop the impacters onto the rings and then cut tension specimens from the rings. To determine the actual effect of the propellent, some of the rings were filled with inert solid propellent. Even though the rings were smaller than a FWC, it was believed that the impact damage in the rings would be the same as that in a FWC because the layup and thickness of the rings and FWC's were the same. It was assumed that the hoop stresses at failure would be about the same for a FWC with biaxial stress and the specimens with uniaxial stress.

In the first series of impact tests on the rings, a 25.4—mm— (1.0—in.) diameter hemisphere was used for the indenter (tup)[4—6]. The impacters were of various masses and were dropped from various heights to simulate falling tools and equipment. The specimens were radiographed before being loaded to failure. The extent of impact damage increased with increasing impact force, and the residual tension strength decreased accordingly. For impact forces around 76 kN (17 kips), strengths were reduced as much as 30% without damage being readily visible on the surface. The resin was removed from several specimens following impact, revealing broken fibers. The locus of the broken fibers resembled cracks on a macroscopic scale. The damage size (breadth and depth) was calculated assuming Hertzian contact and maximum stress criteria. The damage was represented as a surface crack, and residual tension strength was calculated using surface crack analysis[6,7]. The predictions and experiments were in reasonably good agreement. The size and nature of the damage was difficult to determine nondestructively[3,8—10]. Thus, a number of specimens were damaged by simulated impacts and deplied to verify the predictions of damage[11]. The impacts were simulated by quasi—statically pressing the indenter against the face of specimens that had been cut from an actual FWC. These measurements of damage size were also in good agreement with calculations made assuming Hertzian contact and maximum stress criteria.

Because of concern about reduction in strength due to nonvisible impact damage, additional impact tests were conducted on the remaining filled and empty rings to determine the relevance of impacter shape to nonvisible damage and the associated reduction in strength. The following indenters were used: a 12.7—mm— (0.5—in.) diameter hemisphere, a sharp corner, and a 6.3—mm— (0.25—in.) diameter bolt—like rod. Only the height from which the impacter was dropped was varied —— not the mass[12]. Because no rings remained, impacts with the rod were simulated by quasi—statically pressing the rod against the face of specimens that had been earlier cut from an empty ring. The specimens were then loaded uniaxially in tension to failure. The effects of indenter shape on impact force, damage size, damage visibility, and residual tensile strength were calculated using the previously developed analyses[4—6]. Factors of safety for strength reduction with nonvisible damage were calculated in terms of impact energy.

Although this investigation was made using uniaxially loaded specimens, an actual FWC with damage and delaminations introduced in critical regions was pressure tested to failure by Hercules at the end of the program. Based on results from the present investigation and work done by Hercules, delaminations and damage were selected that were large enough to be detectable but not large enough to reduce the factor of safety below the minimum of 1.4. In the membrane region, delaminations were as large as 1.948 m^2 (3019 $in.^2$), surface cuts were as deep as 1.1 mm (0.045 in.), and impacts were made to give at least barely visible damage on the surface. Three indenters were used, each with a different level of kinetic energy: a sharp corner with 13 J (9.4 ft—lbf) of energy, a 12.7—mm— (0.5—in.) diameter hemisphere with 26 J (19 ft—lbf) of energy, and a 25.4—mm— (1.0—in.) diameter hemisphere with 110 J (82 ft—lbf) of energy. The burst pressure was 10.01 MN/m^2 (1452 psi), and the corresponding factor of safety was 1.54, about 10% greater than the required 1.4. Pressure tests of undamaged FWC's gave similar factors of safety.

Even though the FWC design was primarily governed by internal pressure, the booster motors of the Space Shuttle are also subjected to bending when the main engines of the orbiter ignite, causing relatively large compression stresses in the aft FWC's. Two FWC's without damage or defects were loaded in bending to failure by Hercules. The factors of safety corresponding to failure were 1.68 and 1.73, considerably greater than those associated with internal pressure but probably not large enough to ignore the effects of damage on compression strength.

Certain commercial materials are identified in this paper in order to specify adequately which materials were used. In no case does such identification imply that the materials are necessarily the only ones or the best ones available for the purpose.

Experiments

The material, test apparatus, and procedure are

reviewed here for the convenience of the reader. They have been described in more detail elsewhere[2,4–6,11,12].

Material

The 0.76–m– (30–in.) diameter, 2.13–m– (84–in.) long cylinder was made by Hercules Inc. to represent the membrane region of a FWC. The thickness of the cylinder was the same as that of a FWC, 36 mm (1.4 in.). The hoop and helical fiber directions of the cylinder were rotated 90° relative to those of the FWC to provide straight specimens for uniaxial loading in the hoop direction of the FWC. The directions of the hoop (0°) and helical (±56.5°) layers are shown in Figure 1 for the cylinder. (The 0° and ±56.5° directions are measured relative to the

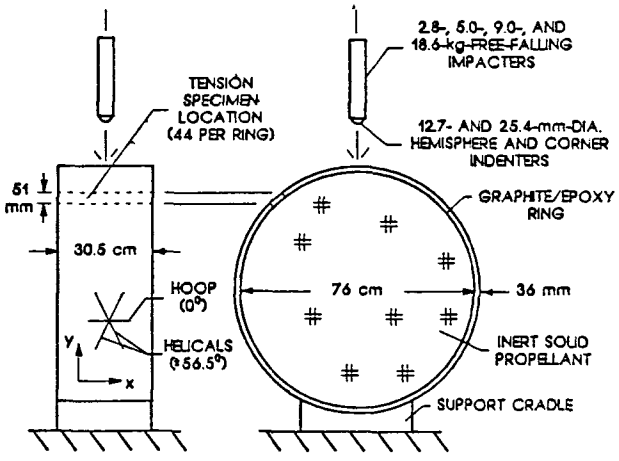

Figure 1. Impact Tests of Graphite/Epoxy rings

longitudinal direction of the cylinder.) From outside to inside, the orientations of the layers were $\{(\pm 56.5)_2/\ 0/\ [(\pm\underline{56.5})_2/\ 0]_3/\ [(\pm 56.5)_2/\ 0]_7/\ (\pm 56.5/\ 0_2)_4/\ (\pm 56.5)_2/\ \underline{0/90}\}$, where the underlined $\pm\underline{56.5}$ helical layers are about 1.6 times as thick as the other helical layers and the $\underline{0/90}$ layer at the inner surface is a plane weave cloth.

The ±56.5° layers were filament wound using a wet process. The fibers and winding resin were Hercules Inc.'s AS4W–12K graphite and HBRF–55A epoxy, the same as the FWC's. The 0° layers could not be filament wound with the available equipment; instead, they were laid by hand using prepreg tape made of the same fibers and a compatible epoxy, Hercules Inc.'s MX–16. The elastic constants of the laminate, which were calculated using lamination theory, are given in Table 1. The x– and y–directions in the subscripts of the elastic constants correspond to the axial and hoop directions of the cylinder, respectively. See Figure 1. The z–direction corresponds to the radial (thickness) direction of the cylinder and FWC. The values of E_z, G_{zx}, ν_{xz}, and ν_{yz} were assumed to be equal to those of E_{22}, G_{12}, ν_{12}, and ν_{12}, respectively.

Property	Value
E_x, GPa (Msi)	30.6 (4.44)
E_y, GPa (Msi)	39.0 (5.66)
E_z, GPa (Msi)	4.15 (0.603)
G_{xy}, GPa (Msi)	19.7 (2.86)
G_{zx}, GPa (Msi)	4.38 (0.635)
ν_{xy}	0.351
ν_{yx}	0.447
ν_{xz}	0.271
ν_{yz}	0.271

TABLE 1. Elastic Constants of FWC

Inert solid propellent was cast into some of the rings. The masses of an empty and a filled ring were 40 kg (89.1 lbm) and 288 kg (635 lbm), respectively.

Test Apparatus and Procedure

Impact Tests. The rings were impacted by free–falling masses. See Figure 1. During impacts, the rings lay on a thin rubber sheet in a shallow aluminum cradle. The bottom of the empty rings was secured to the concrete floor with a cross–bar to prevent the rings from "leaping" off the floor when impacted. Each ring was impacted every 59 mm (2.3 in.) of outer circumference, giving 44 impact sites. The damaged regions did not overlap. Some sites on each ring were not impacted but reserved as undamaged specimens for determining mechanical properties. The cut edges of each specimen were ground flat and parallel so that the width and length of the specimens were 51 mm (2.0 in.) and 31 cm (12 in.), respectively. The center of each specimen was made to coincide with an impact site.

The free–falling impacters were 51–mm– (2–in.) diameter steel rods with indenters of various shapes attached to one end. Four rods of different lengths were used to give masses of 2.8, 5.0, 9.0, and 18.6 kg (6.1, 11.1, 19.9, and 41.1 lbm), including the indenter. A piezoelectric accelerometer and four strain gages were embedded in the rods immediately behind the indenter for measuring acceleration and impact force, respectively. The indenters were a 12.7–mm– (0.5–in.) and a 25.4–mm– (1.0–in.) diameter hemisphere and a corner made of three orthogonal surfaces. The tip of the corner had a radius of about 0.25 mm (0.01 in.).

For the 25.4–mm– (1.0–in.) diameter hemisphere, all four impacters were dropped on one empty and one filled ring. Drop heights were varied to give kinetic energies from 41 to 446 J (30 to 329 ft–lbf). The contact area was recorded by placing sheets of white bond paper and carbon paper on the rings. For the 12.7–mm– (0.5–in.) diameter hemisphere and the corner, the 5.0 kg (11.1 lbm) impacter was dropped on one empty and one filled ring. Drop heights were varied from 36 to 274 cm (14 to 108 in.) to give kinetic energies from 17 to 136 J (13 to 100 ft–lbf).

Simulated Impact Tests. Because of a lack of whole rings, some impact tests were simulated by slowly pressing indenters against the face of small specimens while controlling the magnitude of the force. The impacts were not made by dropping weights because of a potential difference between the dynamic response of the ring and that of a small specimen. The force was applied with a 500–kN hydraulic testing machine. The indenters were attached to one grip of the testing machine, and the specimens lay on a steel platen attached to the other grip.

In the first case, simulated impact tests were conducted on 30.5–by–30.5–cm (12–by–12–in.) FWC pieces to better determine the nature of the fiber damage and to verify predictions of damage size. The pieces were from a FWC that had essentially the same layup as the cylinder but was completely wet–wound with AS4W–12K graphite and HBRF–55A epoxy. Thirty six 38–by–38–mm (1.5–by–1.5–in.) specimens were cut from each FWC piece after the forces were applied. The contact sites were at the center of the specimens. The specimens were heated to 400° C (752° F) for 60 minutes to remove most of the epoxy. Following pyrolysis, the layers were separated and examined with an optical microscope to measure the

extent of fiber damage. Hemispherical indenters of three diameters were used: 12.7, 25.4, and 50.8 mm (0.50, 1.0, 2.0, in.). The average contact pressure to cause visible surface damage was about 648 MPa (94.0 ksi). Thus, contact pressures were selected between 408 and 742 MPa (59.2 and 108 ksi) so that maximum nonvisible damage was included. The corresponding forces, which were calculated assuming Hertzian contact, varied from 4.18 to 400 kN (0.94 to 90 kips). The smallest force corresponds to the smallest indenter and the largest to the largest indenter.

In the second case, nine of the 51— mm (2.0—in.) by 30.5—cm (12—in.) tension specimens that were reserved for tests to determine mechanical properties were used instead for simulated impact tests with a rod shaped indenter. The rod had a diameter of 6.3 mm (0.25 in.). The corner of the rod (intersection of the side and end) had a radius of 1.3 mm (0.05 in.) to simulate the end of a bolt. Stroke (displacement of the indenter) was programmed to increase linearly with time. The maximum strokes were 3.4, 6.5, and 9.5 mm (0.135, 0.255, and 0.375 in.) for three specimens each.

X—Ray Tests. The impacted face of each specimen (including those with simulated impacts using the rod) was soaked in a zinc iodide penetrant for 30 sec, and radiographs were made from the impacted side and the edge. The penetrant was contained by a circular dam on the surface of the specimen. The depth of impact damage in the radiographs was measured. The pieces from the FWC that were subjected to simulated impacts and deplied were not radiographed.

Residual Strength Tests. After the specimens were X—rayed, circular arcs were ground into the specimens' edges to reduce the width in the test section to 33 or 38 mm (1.3 or 1.5 in.). See Figure 2. The specimens were uniaxially loaded to failure

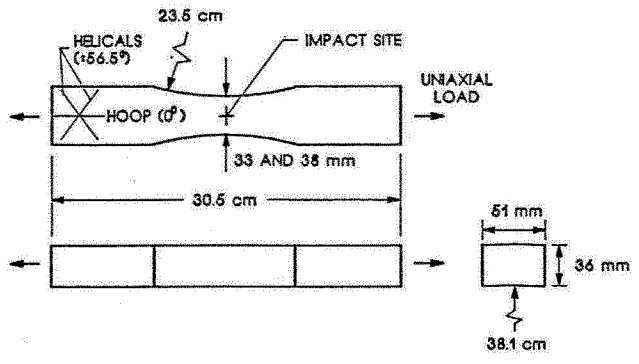

Figure 2. Tension Specimen

in tension with a 445—kN— capacity (100 kips) hydraulic testing machine. Stroke was programmed to increase with time at the rate of 0.0076 mm/sec (0.0003 in./sec). Time to failure was several minutes at this rate. Hydraulically actuated grips that simulate fixed—end conditions were used. Otherwise, uniaxial loading would cause bending because the FWC laminate is not symmetrical. In order to hold onto the specimens, the grips generated very high contact pressure on the faces of the specimens. Without reducing the width in the test section, the failure of specimens with small damage appeared to originate at the edge of the grips where the contact pressure was highest.

Results

The mass of an empty ring is about seven times that of a ring filled with inert solid propellent. Thus, it was desirable to present the results in terms of a parameter that takes into account the mass of the target as well as that of the impacter. Such a parameter, the effective kinetic energy, was derived assuming Hertzian contact and Newtonian mechanics. The first part of the results section verifies these equations.

Hertzian Contact

For Hertzian contact between an isotropic sphere and a transversely isotropic semi—infinite body[13], the contact radius is

$$r_c = (F\ R_i/n_0)^{1/3} \qquad (1)$$

where R_i is the radius of the sphere, F is the contact force, and n_0 is a function of the elastic constants of the sphere and semi—infinite body given by equation (A1) in the Appendix.

The local displacement or indentation of the semi—infinite body is

$$u_i = R_i^{-1/3}\ (F/n_0)^{2/3} \qquad (2)$$

Equation (2) is accurate only when $u_i << R_i$.

The impact force increases with time to a maximum value F_{max} and then decreases to zero, much as a haversine function. The time for the impact force to reach a maximum value increases with increasing impacter mass. For the filled and empty rings, the time varied between about 0.5 to 1 millisecond for the range of impacter masses. The measurements of contact radius are plotted against F_{max} in Figure 3 for the 25.4—mm— (1.0—in.) diameter hemisphere. Different symbols were used to

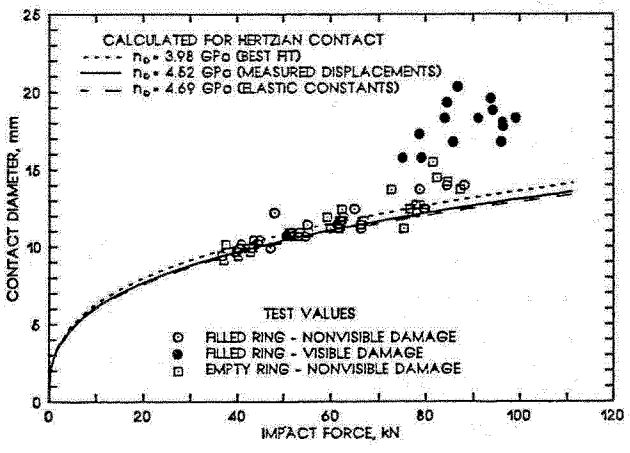

Figure 3. Contact Diameter versus Impact Force for 25.4—mm—dia. hemisphere

differentiate between the filled and empty rings and to indicate when impacts made visible craters. Hereafter, craters will be referred to as visible damage. For the empty ring, contact area was inadvertently not recorded for the impacts that made visible damage. For $F_{max} < 75$ kN (17 kips), the damage was not visible. For F_{max} slightly above 75 kN (17 kips), the craters were very shallow but perceptible. The depth of the craters increased with increasing F_{max}. Equation (1) is also plotted in Figure 3 for three different values of n_0: one value calculated using equation (A1) in the Appendix and the elastic

constants in Table 1, another calculated using equation (2) and measured displacements of the FWC pieces that were subjected to simulated impacts, and one calculated to best fit the measurements of contact radius without visible damage. In using equation (A1) to calculate n_0, transversely isotropic properties were calculated by averaging the x— and y—direction properties in Table 1. The curves and test data without visible damage in Figure 3 agree quite well. When the impacts made visible damage, the contact radius is underestimated by equation (1).

Relationship between Mass, Velocity, and Impact Force

Assuming Hertzian contact and Newtonian mechanics, the following relationship was derived between the maximum impact force, impacter mass, composite ring mass, and impacter velocity[12].

$$\frac{2}{5} R_1^{-1/3} n_0^{-2/3} F_{max}^{5/3} + \frac{1}{2} k_b^{-1} F_{max}^2 - KE_{eff} = 0 \quad (3)$$

where

$$KE_{eff} = \frac{1}{2} M v_1^2 \quad (4)$$

M is the effective mass defined by

$$M = [m_1^{-1} + (m_2/4)^{-1}]^{-1} \quad (5)$$

v_1 is the velocity of the impacter, m_1 is the mass of the impacter, and $m_2/4$ is the effective mass of the ring (including the solid propellent). The ring is assumed to initially be at rest.

The relative displacement of the ring and impacter was written as

$$u = u_b + u_i \quad (6)$$

where u_i is the local displacement of the ring defined by equation (2) and u_b is the beam type displacement of the ring defined by

$$u_b = F/k_b \quad (7)$$

Measured values of F_{max} are plotted against KE_{eff} in Figure 4 for the 25.4—mm— (1.0—in.) diameter hemisphere. Each symbol is an average of several tests. The threshold value of KE_{eff} for nonvisible damage is labeled. The values of F_{max} for the empty and filled rings coalesce quite well for the same value of KE_{eff}. Values of F_{max} calculated with equation (3) and $n_0 = 4.52$ GPa (656 ksi) are also plotted. Curves are shown for three values of ring stiffness: $k_b = \infty$, 6.34 MN/m (36.2 kips/in.), and 5.08 MN/m (29.0 kips/in.). For $k_b = \infty$, the ring does not deflect in a global sense as a beam. The last two values of k_b were measured by quasi statically pressing the hemisphere against a filled ring and an empty ring, respectively. When the damage was not visible, the calculated curve for $k_b = \infty$ agrees with the test results quite well. But when damage was visible, the actual impact forces are less than the calculated values, and the difference increases with increasing K_{eff}. Values of F_{max} calculated with the quasi—static values of k_b are much too small. Thus, the quasi—static values of k_b greatly overestimate the

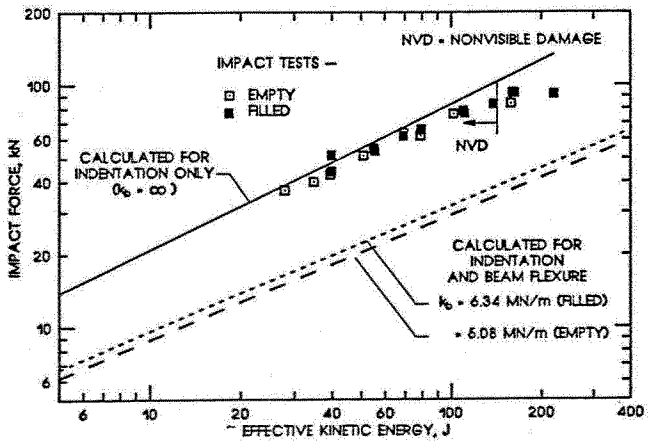

Figure 4. Impact Force Versus Effective Kinetic Energy for 25.4—mm—dia. Hemisphere

global displacement of the rings during impact.

Values of F_{max} are plotted against KE_{eff} in Figure 5 for the 12.7— and 25.4—mm— (0.5— and

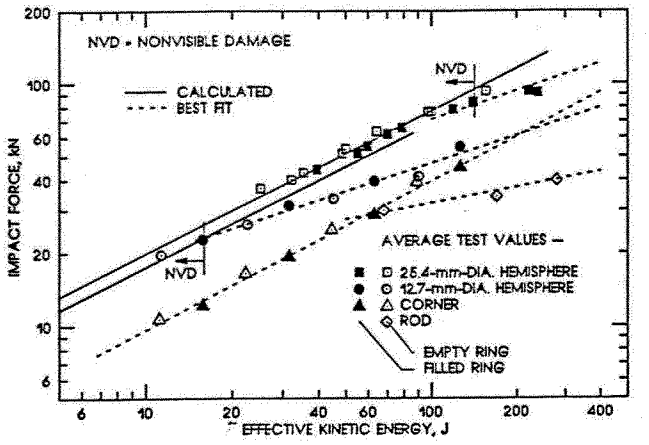

Figure 5. Effect of Impacter Shape on Impact Force

1.0—in.) diameter hemisphere, the corner, and the rod. For the simulated impacts with the rod, the area under the load—displacement curve was used for KE_{eff}. Each symbol is an average of several tests. Thresholds for nonvisible damage are indicated for the hemispheres. The corner and rod made visible damage in all tests. The dashed lines were fit to the test data with visible damage. Again the values of F_{max} for the empty and filled rings coalesce quite well for the same value of KE_{eff}. For the hemispheres, F_{max} increases with increasing radius for a given KE_{eff}. For the range of KE_{eff} values investigated, values of F_{max} are lower for the corner and rod than for the hemispheres. After a critical force was exceeded, the rod acted like a punch and penetrated deeply into the composite. Because of the large displacements, the work increased rapidly with force. Thus, the slope of the test data for the rod is the smallest. Because of the corner's profile, the resistance to penetration increased rapidly with increasing penetration. Thus, the slope of the test data for the corner was as large as that for the hemispheres without visible damage. The solid lines for the hemispheres were calculated with equation (3). The calculations were made using k_b = 219 MN/m (1250 kips/in.) and $n_0 = 4.52$ GPa (656 ksi). This value of k_b was chosen to give the best

agreement between equation (3) and the test data with nonvisible damage. Even though $k_b < \infty$, it is still very large compared to static values, and the term containing k_b in equation (3) contributes very little to KE_{eff}. The values of F_{max} calculated with equation (3) agree quite well with the test values for both hemispheres, when the damage is not visible. When the damage is visible, the calculated values of F_{max} are greater than the test values.

Damage

Radiographs (edge views) of damage for the various indenters are shown in Figure 6. These

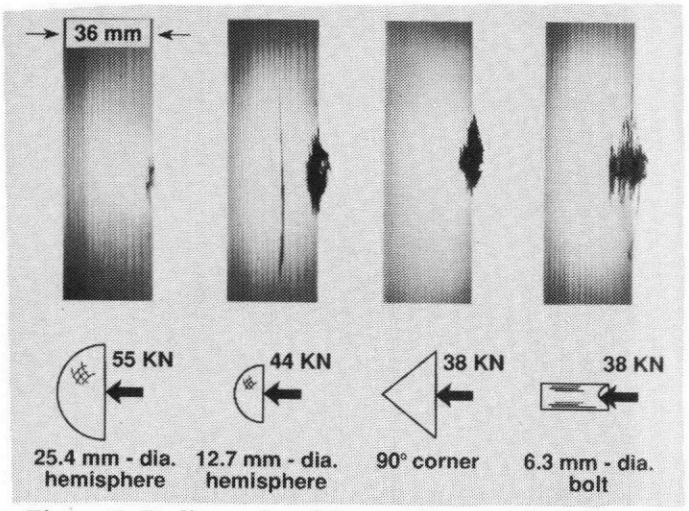

Figure 6. Radiographs of Impact Damage for Various Indenters

impact tests were conducted early in the investigation when the specimens lay on inert solid propellent. The kinetic energy of the impacter was 272 J (200 ft—lbf). The corresponding impact forces are shown for each indenter. Indenter shape had a strong effect on the appearance of the damage.

The maximum depth of damage in radiographs is plotted against KE_{eff} in Figure 7 for the various

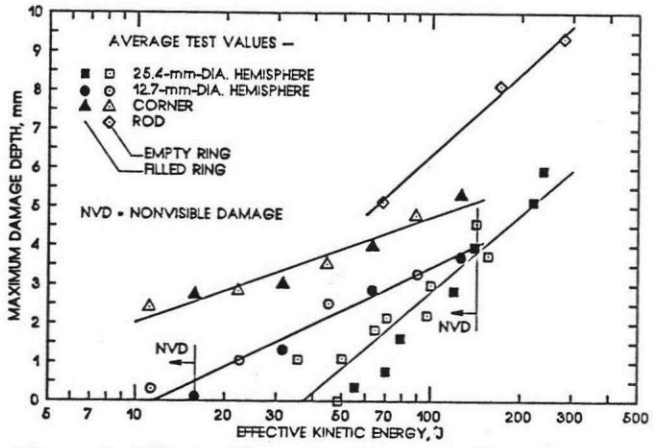

Figure 7. Effect of Impacter Shape on Max. Damage Depth in Radiographs

indenters. For the hemispheres and corner, the impacts were made to the rings. For the rod, the impacts were simulated, and the area under the load—displacement curve was used for KE_{eff}. Filled and empty symbols differentiate between filled and empty rings. Except for the 25.4—mm— (1.0—in.) diameter hemisphere, the data for the filled and empty rings coalesce quite well for a given value of KE_{eff}. For the 25.4—mm— (1.0—in.) diameter hemisphere, the data coalesce for the largest values of KE_{eff} but diverge with decreasing KE_{eff}. For small values of KE_{eff}, the damage was deeper in the empty ring than in the filled ring. For all indenters but the rod, the data also tend to coalesce for the largest values of KE_{eff}. Moreover, for values of $KE_{eff} > 200$ J (272 ft—lbf), the damage could be deeper for the 25.4—mm— (1.0—in.) diameter hemisphere than for the 12.7—mm— (0.5—in.) diameter hemisphere and the corner. The threshold for nonvisible damage is also shown in Figure 7 for the hemispheres. For the 12.7—mm— (0.5—in.) diameter hemisphere, damage is visible on the surface whenever it is deeper than 0.5 mm (0.02 in.). However for the 25.4—mm— (1.0—in.) diameter hemisphere, damage is not visible on the surface until it is deeper than 4.0 mm (0.16 in.).

Residual Tension Strength

When the impacted specimens were loaded to failure in tension, those with very shallow damage (outermost helical layers or less) failed catastrophically in one stage. But, those with deeper damage (one or more hoop layers) failed in two stages: first, the damaged layers failed and delaminated from the undamaged layers (See Fig. 8); and then, with additional load, the undamaged layers failed. The two

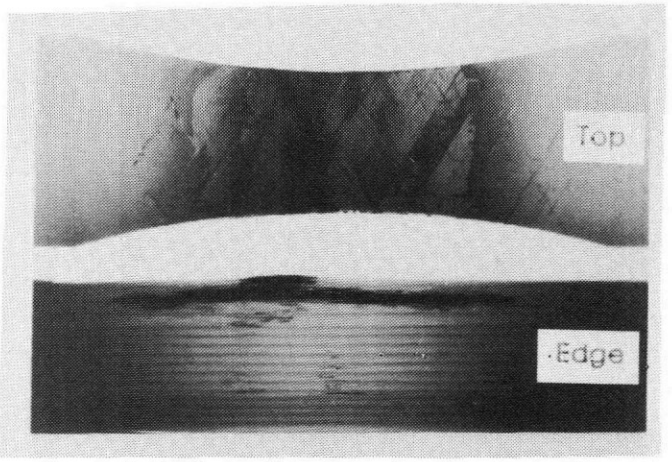

Figure 8. Radiographs of Tension Specimen after Failure of First Ligament

stages of failure were referred to as first— and remaining—ligament failure.

Chatterjee[14] made calculations of the strain energy release rate for the delamination after failure of the first ligament and found that it was large relative to the interlaminar toughness of similar graphite/epoxy laminates. Thus, such a delamination would probably spread throughout a FWC as long as the internal pressure was not reduced.

The stresses for first— and remaining—ligament failure are plotted against KE_{eff} in Figures 9 and 10, respectively, for the various indenters. For the rod, the area under the load—displacement curve was used for KE_{eff}. Filled and empty symbols are used to differentiate between the filled and empty rings. For a given value of KE_{eff} and indenter, the failure stresses do not coalesce as well as the values of F_{max} in Figure 5. For the 25.4—mm— (1.0—in.) diameter hemisphere, failure stresses are lower for the empty ring than the filled ring. But for the 12.7—mm— (0.5—in.) diameter hemisphere and the corner, failure stresses are lower for the filled ring than the empty ring. Thus, the differences are not likely due to the

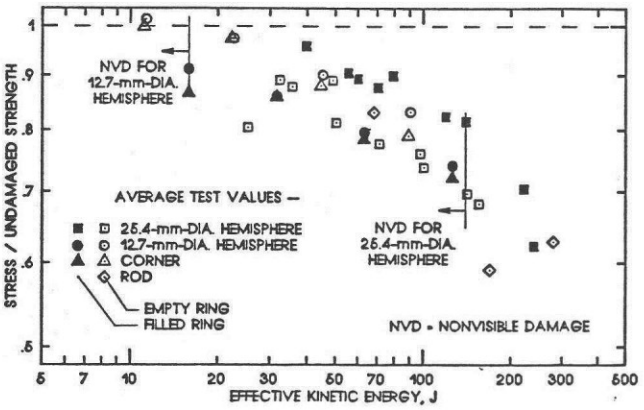

Figure 9. Effect of Indenter Shape on Stress for Failure of First Ligament

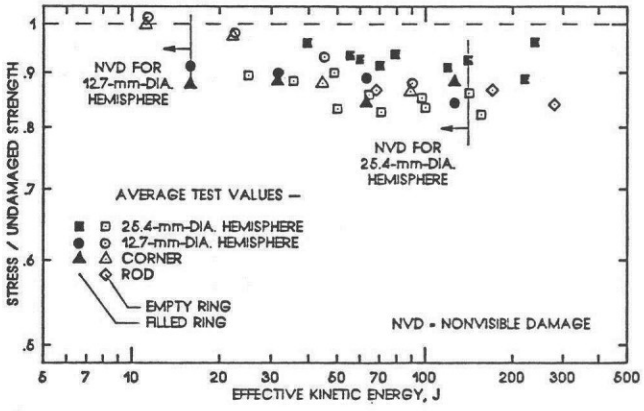

Figure 10. Effect of Indenter Shape on Stress for Failure of Remaining Ligament

presence of the inert solid propellent. Unexpectedly, the stresses for first– and remaining–ligament failure only vary 10–15% with indenter shape for a given value of KE_{eff}. For the two hemispheres, values of KE_{eff} for nonvisible damage are also shown in Figure 9. The failure stresses associated with nonvisible damage decreased with increasing diameter. For the 25.4–mm– (1.0–in.) diameter hemisphere, the stress for first–ligament failure with nonvisible damage is as low as 70% of the undamaged strength.

Analysis and Discussion

Fiber Damage

Photographs of the outermost 9 layers from a deplied specimen are shown in Figure 11. This specimen is one of those taken from a piece of an actual FWC. It was subjected to a simulated impact using a 50.8–mm– (2.00–in.) diameter hemisphere, producing a contact force of 267 kN (60.0 kips). The layers contain broken fibers, the loci of which resemble cracks on a macro scale. Broken fibers were visible in the 15 outermost layers, of which the outermost 9 are shown here. The cracks are mostly parallel to the direction of fibers in the neighboring layers. When the direction of fibers on opposite sides of a layer were not equal, the direction of the cracks in the intermediate layer wandered between the direction of the fibers in the neighboring layers. Several specimens were not deplied but were sectioned normal to the plane of the laminate and examined using a scanning electron microscope[11]. The sections revealed matrix cracks in planes of maximum shear stress that passed through broken fibers. The ends of broken fibers were displaced relative to one another as though the fibers also broke in shear. Probably shear failure of the matrix precipitated the failure of the fibers.

The maximum depth of broken fibers divided by contact radius r_c are plotted against average contact pressure p_c in Figure 12 for hemispherical indenters with three diameters: 12.7 , 25.4 , and 50.8 mm (0.5, 1.0, and 2.0 in.). The depths were determined from

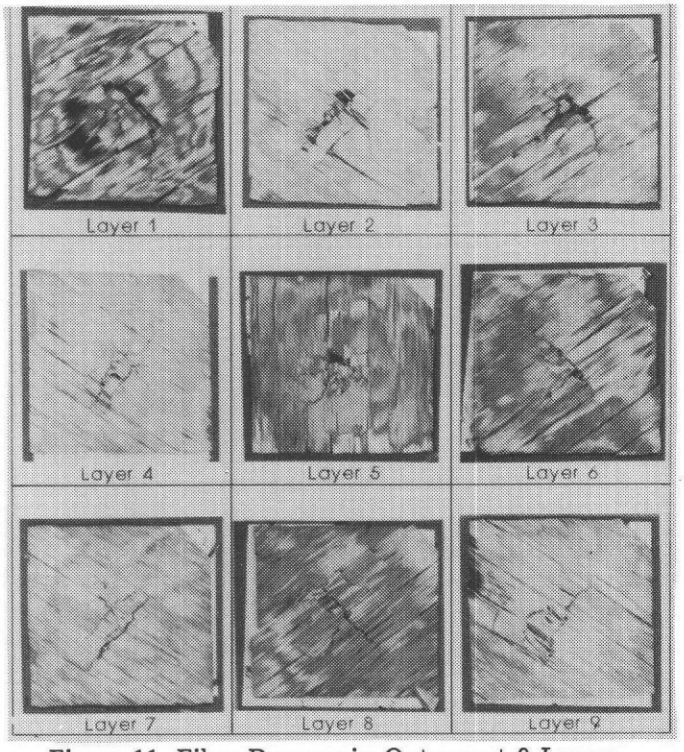

Figure 11. Fiber Damage in Outermost 9 Layers

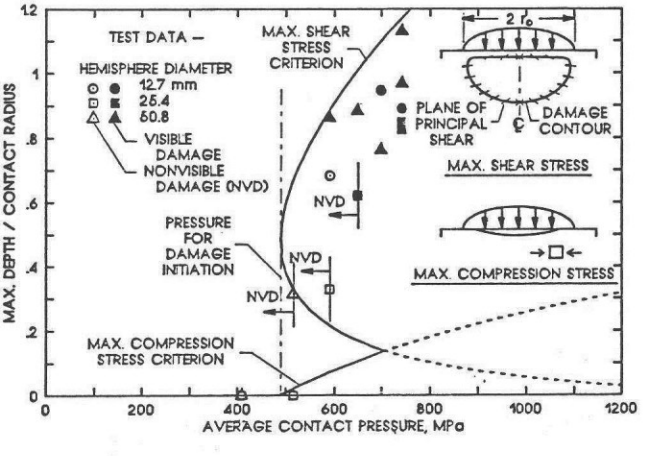

Figure 12. Maximum Damage Depth Versus Contact Pressure

deplied specimens like that in Figure 11. Values of r_c were calculated using equation (1) with $n_0 = 4.52$ MPa (656 ksi), and values of p_c were calculated

using $p_c = F_{max}/(\pi r_c^2)$. The filled and empty symbols distinguish between visible and nonvisible damage. The values of p_c for nonvisible damage decrease with increasing R_i. Equation (1) can also be written

$$r_c = R_i p_c/(\pi n_0) \quad (8)$$

Thus, r_c increases in proportion to R_i for a given value of p_c, and the values of r_c for the smallest hemisphere are generally one fourth those for the largest hemisphere. For this reason, the absolute depth of damage for the smallest hemisphere is generally one fourth that for the largest hemisphere. This variation in damage size with R_i may cause the decrease in p_c with increasing R_i for nonvisible damage. That is, the size of surface damage, and hence the visibility of the damage, also decreases with decreasing R_i.

For impact tests with the 12.7— and 25.4—mm— (0.5— and 1.0—in.) diameter hemispheres, the values of p_c for nonvisible damage were 719 MPa (104 ksi) and 700 MPa (102 ksi), respectively. These values of p_c are only about 13% less than those in Figure 12 for corresponding diameters. Also, damage depths in Figures 7 and 12 are in reasonably good agreement, more so for the 25.4—mm— (1.0—in.) diameter hemisphere than the 12.7—mm— (0.5—in.) diameter hemisphere[12].

For Hertzian contact between an isotropic sphere of radius R_i and a semi—infinite transversely isotropic body[13], the contact pressure on the surface of the semi—infinite body is given by

$$p(r) = \frac{3}{2} p_c (1 - r^2/r_c^2)^{1/2} \quad (9)$$

where r is the radius measured from the center of the contact site (polar coordinate). Notice that the pressure at the center ($r = 0$) is 50% greater than the average value.

Using the theory of elasticity, Love[15] obtained a closed form solution for the internal stresses in a semi—infinite, isotropic body produced by the "hemispherical" pressure given by equation (9). Even though the composite is made of orthotropic layers, results from Love's solution should at least be applicable in a qualitative sense if r_c is much greater than the thickness of the layers. Damage contours were calculated with stresses from Love's solution, a maximum shear stress criterion, and a maximum compression stress criterion in the plane of the laminate. A compression allowable of $\sigma_{cu} = 587$ MPa (85.1 ksi), a shear allowable of $\tau_u = 228$ MPa (33.0 ksi), and a value of $\nu = 0.3$ were used. The compression allowable of 587 MPa (85.1 ksi) was calculated by multiplying the compression failing strain by Young's modulus of the laminate. The shear allowable of 228 MPa (33.0 ksi) was chosen to give an upper bound to the damage depths in Figure 12. The plane of maximum shear stress varies along the damage contour. At the center ($r = 0$), the plane of maximum shear is at 45° to the plane of the laminate. (See the sketch in Fig. 12.) Near the extremity of the contact region ($r = r_c$), the plane of maximum shear stress is nearer the plane of the laminate. The maximum depths of the contours divided by r_c are plotted against p_c in Figure 12. The values of r_c were calculated as were those of the test data. For the maximum shear stress criterion, the damage initiates below the surface at a depth of $0.482\, r_c$ when $p_c = 490$ MPa (71.1 ksi), which corresponds to $p_c = 2.15\, \tau_u$. For the maximum compression stress criterion, the damage initiates at the surface when $p_c = 487$ MPa (70.6 ksi), which corresponds to $p_c = 0.833\, \sigma_{cu}$. The envelope of the two maximum stress criteria is represented by the solid lines. The damage far below the surface corresponds to the maximum shear stress criterion, and the damage near the surface corresponds to the maximum compression stress criterion. The maximum stress criteria represent the data quite well considering that the composite is neither homogeneous nor isotropic. Widths of the calculated contours were approximately 1.6 times the depth, whereas those from the tests were 2 to 3 times the depth. This discrepancy is probably due to the anisotropy the composite.

Transverse compression tests of disks of several diameters gave a value of $\tau_u = 310$ MPa (45.0 ksi), which is about 50% greater than that used to calculate the curve in Figure 12. Use of the larger value of τ_u would move the threshold from 490 MPa (71.1 ksi) to 668 MPa (96.9 ksi) and give a lower bound to the test data. Instead, one would expect the value of τ_u from the compression tests to give values of damage depth that agree with those in Figure 12 on the average. The discrepancy is likely due to the use of isotropic[15] rather than anisotropic theory of elasticity to calculate internal stresses.

As noted previously, all impacts by the corner and rod caused visible damage on the surface. Contact pressures (averaged over the contact surface) for all tests with the corner and rod exceeded those for the hemispheres to cause visible damage, particularly the corner[12]. Thus, average contact pressure may be a good indicator of damage initiation. One cannot be certain because the largest pressure within the contact region does vary with indenter shape. For example, equation (9) indicates that the maximum pressure for a hemisphere is 1.5 times the average and occurs at the center. But, the contact pressure tends to be unbounded near the edge of a rod with a flat end. This unbounded pressure gives rise to unbounded stresses that cause a punch type behavior.

Residual Tension Strength

The stresses for first—ligament failure are critical because they are either less than or equal to those for remaining—ligament failure. Thus, only the analysis of stresses for first—ligament failure will be reviewed. The impact damage was represented as a semi—elliptical surface crack, and the stress for failure of the first ligament was calculated using surface crack analysis[4—7]. The crack was assumed to be in a plane normal to the hoop direction. The depth of the equivalent crack a was calculated with stresses from Love's solution and the maximum shear stress criterion with $\tau_u = 228$ MPa (33 ksi) and $n_0 = 4.52$ GPa (656 ksi). The length of the equivalent crack $2c$ was assumed to be two times the depth (semi circular). At failure, the critical stress intensity factor[16] or fracture toughness K_q is given by

$$K_q = S_{xf} (\pi a/Q)^{1/2} f(a/h, a/c, c/W, \phi) \quad (10)$$

where S_{xf} is the laminate stress for failure of the first ligament, Q is the shape function, and $f(a/h, a/c, c/W, \phi)$ is the correction factor for finite thickness h and width W. The parametric angle ϕ was taken as 0° or 90°, whichever gave the largest value of the correction factor. The fracture toughness K_q of the laminate was calculated using the elastic constants, the failing strain of the fibers, and a general fracture toughness parameter[4—6]. For a crack whose plane is normal to the 0° direction of the cylinder, the

result was $K_Q = 0.949$ GPa$\sqrt{mm}$ (27.3 ksi$\sqrt{in.}$).

For shallow surface cracks or impact damage, equation (10) gives strengths that are greater than those from tests. To correct this discrepancy, a line was drawn tangent to equation (10) and passing through the undamaged strength at a depth corresponding to the outermost hoop layer[6]. (Strengths were not reduced unless the hoop layers were damaged.)

Values of S_{xf} are plotted against KE_{eff} in Figure 13 for the 12.7— and 25.4—mm— (0.5— and

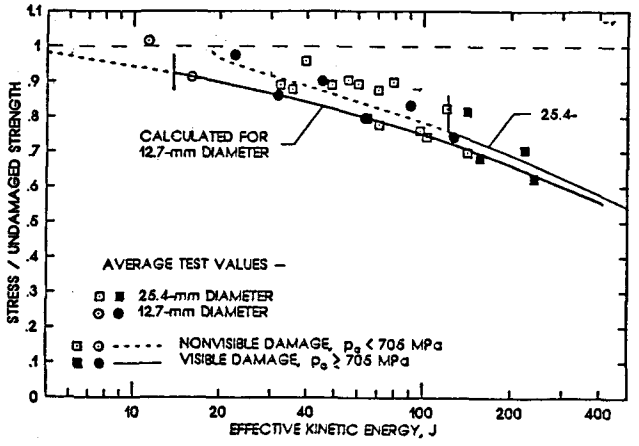

Figure 13. Effect of Hemisphere Diameter on Stress for First—Ligament Failure

1.0—in.) diameter hemispheres. The values of S_{xf} were divided by the undamaged strength $F_{tu} = 345$ MPa (50.1 ksi). The open and filled symbols for the test data differentiate between visible and nonvisible damage. The curves, which were calculated with equation (10), were dashed to indicate nonvisible damage, $p_c < 705$ MPa (102 ksi), and solid to indicate visible damage, $p_c \geq 705$ MPa (102 ksi). The predictions and tests are in reasonably good agreement, even when damage was visible. In Figures 3 and 5, F_{max} was overestimated and r_c was underestimated when damage was visible. Perhaps these discrepancies offset one another.

Values of S_{xf} calculated with equation (10) are plotted against KE_{eff} in Figure 14 for hemispherical

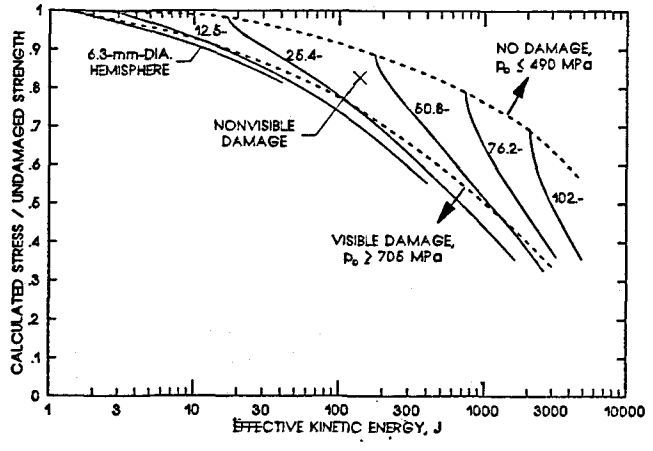

Figure 14. Calculated Stress for First—Ligament Failure for Various Hemisphere Diameters

diameters ranging from 6.3 to 102 mm (0.25— and 4.0—in.). Again, the values of S_{xf} were divided by F_{tu}. For a given value of R_i, the value of r_c increases with increasing KE_{eff}. The calculations were terminated at the lower ends of the curves when r_c reached R_i. (Values of $r_c > R_i$ are physically unrealizable.) The locus of S_{xf} values for $p_c = 490$ MPa (71.1 ksi) and 705 MPa (102 ksi) are plotted as dashed curves. These curves represent the thresholds for damage and for nonvisible damage, respectively, and divide the graph into regions of no damage, nonvisible damage, and visible damage. If the FWC must have sufficient strength to accommodate nonvisible damage, then the allowable stress must not be above the corresponding dashed curve for all possible values of KE_{eff}. Otherwise, nonvisible damage would cause failure. If the allowable stress is chosen from the curve for nonvisible damage, impacts causing visible damage could cause failure, depending on impacter shape. Thus, all visible damage would have to be detected and repaired.

The hemisphere diameter $2R_i$ is plotted against KE_{eff} in Figure 15 for the values of p_c that

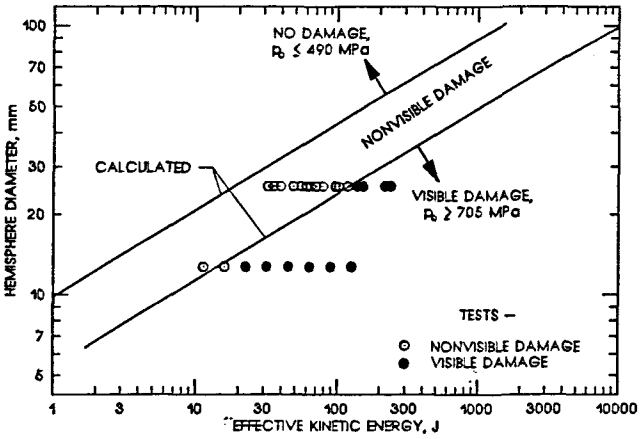

Figure 15. Hemisphere Diameter and Effective Kinetic Energy to Cause Damage

correspond to the thresholds for initiating damage and for nonvisible damage in Figure 14. As in Figure 14, the curves divide the graph into regions of no damage, nonvisible damage, and visible damage. Combinations of R_i and KE_{eff} in the "no damage" region do not cause damage, similarly for the "nonvisible damage" and "visible damage" regions. Along the curves for damage initiation and nonvisible damage, KE_{eff} increases approximately with R_i^3. Thus, for large R_i, very large values of KE_{eff} are necessary to initiate damage and to cause visible damage. But as shown in Figure 7, the depth of nonvisible and visible damage can be nearly equal for 12.7— and 25.4—mm— (0.5— and 1.0—in.) diameter hemispheres for the same value of KE_{eff}. Test data for the 12.7— and 25.4—mm— (0.5— and 1.0—in.) diameter hemispheres are plotted in Figure 15 for comparison. The filled and empty symbols differentiate between visible and nonvisible damage. The calculations and tests agree quite well.

The factor of safety for impact damage is given by the ratio of undamaged strength to damaged strength. Reciprocals of the strength ratios for the test data in Figure 9 are plotted against KE_{eff} in Figure 16. The reciprocal of the dashed curve for $p_c = 705$ MPa (102 ksi) in Figure 14 is also plotted. This curve corresponds to a factor of safety for nonvisible damage. The solid curve passes through the midst of the data and below some of the open symbols for the 25.4—mm (1.0—in.) diameter hemisphere. The dashed curve was

drawn through the locus of highest open symbols using the solid curve as a guide. The factor of safety for the membrane of the FWC, which was 1.4, is shown as a horizontal line in Figure 16. It intersects the dashed

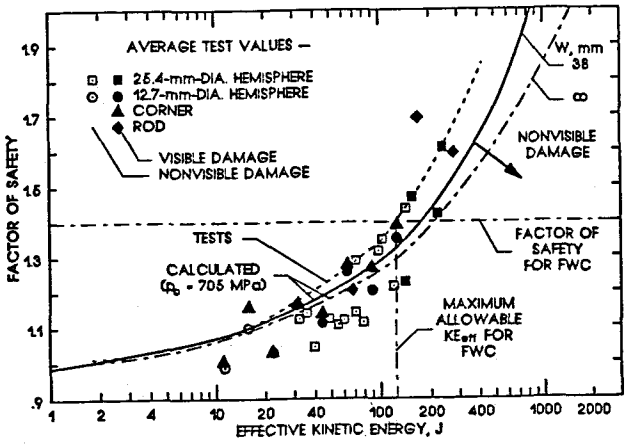

Figure 16. Factor of Safety for nonvisible Damage Versus Effective Kinetic Energy

curve at KEeff = 123 J (91 ft–lbf). Thus, the FWC must be protected for values of KE_{eff} > 123 J (91 ft–lbf).

The specimens in this investigation were 33– and 38–mm wide. The solid curve in Figure 16 was calculated assuming that W = 38 mm. Differences between calculations for W = 33 and 38 mm were insignificant. The dash–dot curve in Figure 16 was calculated for W = ∞, which is more representative of a FWC. The difference between calculations for W = 38 mm and W = ∞ is only significant for very large values of KE_{eff} where the length of the equivalent surface crack in equation (10) exceeds about one half the specimen width.

Consider that the FWC's were to have been manufactured at one location, shipped by truck to another site and loaded with solid propellant, and then shipped by rail to the launch site and assembled. Thus, the FWC's were to be moved many times. Moreover, one empty FWC was dropped onto the floor at the manufacturing plant. Although this investigation was conducted with impacts from small objects like tools and equipment in mind, impacts between a moving FWC and some other rigid or massive object must also be considered. The longest FWC's had a mass of about 4,500 kg (10,000 lbm) empty and about 140,000 kg (300,000 lbm) when filled with propellant. Thus, the potential energy or kinetic energy of one of these FWC's is very large when they are being moved, 44,000 J (33,000 ft–lbf) for an empty FWC lifted 1 m (39 in.). The energy for a filled FWC would be 30 times that for an empty FWC. The results here can be applied directly because the velocity v_1 in equation (4) can be taken as the relative velocity. If the mass of the impacter and the target are very different, the effective mass is equal to the smallest of the two masses. (See equation (5).) On the other hand, If the mass of the impacter and the target are equal, the effective mass is equal to one half that of one of the masses. Like the rings, the effective mass of the FWC or the other object would probably be considerably less than the resting mass. Still, the values of KE_{eff} could be orders of magnitude times those considered in this investigation. From Figure 16, the factor of safety exceeds two for values of KE_{eff} exceeding 2,000 J (1,500 ft–lbf). Thus, the FWC's must be handled very carefully and probably protected.

The large weight is a hazard even when a FWC is at rest. If a FWC lay on a protuberance, the protuberance would act like the indenter in a simulated impact. For the filled and empty rings, residual tension strengths were equal for impacts and simulated impacts with the 25.4–mm– (1.0–in.) diameter hemisphere when values of F_{max} were equal[4,5]. The weight of an empty FWC is about 44 kN (10 kips), which is about as large as the largest impact forces for all of the indenters except the 25.4–mm– (1.0–in.) diameter hemisphere. (See Figure 5.) The weight of a FWC filled with propellant is about 30 times the weight of an empty FWC, which is much larger than the largest impact force. Thus, care must be taken not to lay FWC's on a hard protuberance.

Concluding Remarks

An investigation was made to determine the effect of low velocity impacts by tools and small equipment on the tension strength of a thick filament–wound case (FWC) for the booster motors of the Space Shuttle. Falling weight impact tests were conducted on rings (short cylinders) that were 30.5–cm (12–in.) long and 36–mm (1.4–in.) thick (actual thickness of FWC). The rings were cut from a 2.13–m– (84–in.) long cylinder that was wet–wound on a 76.2–cm– (30–in.) diameter mandrel using AS4 graphite fibers and an epoxy resin. Some rings were filled with inert solid propellant. Three indenters (tups) were used for the impact tests: a sharp corner and two hemispheres, one hemisphere with a 12.7–mm (0.5–in.) diameter and one with a 25.4–mm (1.0–in.) diameter. Drop height was varied, and, for the 25.4–mm (1.0–in.) diameter hemisphere, mass was also varied. The rings were impacted numerous times around the circumference and then cut into 51–mm– (2–in.) wide tension specimens, each containing an impact site. Because no rings remained, impacts with a 6.3–mm– (0.25–in.) diameter rod were simulated by quasi–statically pressing the rod against the face of surplus specimens that had been earlier cut from an empty ring. The size of the damage and the residual tension strength were measured. The damage was always local to the impact site and never extended into neighboring impact sites.

For the hemispheres, the indentation and contact radius were well represented as Hertzian contact. Assuming Hertzian contact and Newtonian mechanics, a relationship was derived for maximum impact force, effective kinetic energy, and stiffness of the composite ring. The effective kinetic energy accounts for the relative mass of the impacter and composite ring. This relationship modeled the maximum impact force for the hemispherical indenters quite well except when the impacts made visible surface damage (craters). Even then, the effective kinetic energy gave good correlation between maximum impact forces for the empty and filled rings. The damage caused by the hemispheres initiated below the surface before it became visible on the surface. For both hemispheres, the damage initiated when the contact pressure exceeded 490 MPa (71.1 ksi) but did not become visible on the surface until the pressure exceeded 705 MPa (102 ksi). The damage below the surface consisted of broken fibers and epoxy that appeared to fail by shear. The effective kinetic energy to initiate damage below the surface and to cause visible surface damage increased with the diameter of the hemisphere. For the corner and rod, contact pressures were very large and damage was always visible on the surface. Even so, the effective kinetic energy gave good correlation between maximum impact forces for the empty and filled rings.

Under uniaxial tension load in the hoop direction, specimens with very shallow damage (only in the outermost helical layers) failed catastrophically without significant reduction in strength. But, with damaged

hoop layers, the specimens failed in two stages: first, the outermost damaged layers failed and delaminated, and then, with increasing load, the remaining ligament failed. For a given value of effective kinetic energy, the residual strengths did not vary significantly with indenter shape even though the detectability of the damage did vary significantly with indenter shape. The maximum reduction in tension strength for nonvisible damage increased with increasing diameter of the hemisphere. For the 12.7—mm— (0.5—in.) and 25.4—mm— (1.0—in.) diameter hemispheres, the reductions in tension stress for first—ligament failure were about 10 and 30 percent, respectively, for nonvisible damage. Thus, the largest hemisphere was the most critical indenter for reducing strength with nondetectable damage.

Using the maximum impact force, the depth of impact damage caused by the hemispheres was calculated assuming Hertzian contact and a maximum shear stress criterion. Internal stresses were calculated using Love's solution for an isotropic semi—infinite body. The impact damage was represented as a semi—circular surface crack with the same depth as impact damage. Residual tension strengths were then calculated using surface crack analysis. The calculated and test values of residual tension strength were in good agreement, even when the impacts made visible damage. The factor of safety for the membrane of a FWC was 1.4. Assuming that nonvisible damage in the membrane of a FWC must be covered by the 1.4 factor of safety, the corresponding value of effective kinetic energy was 123 J (91 ft—lbf), regardless of the indenter shape. Thus, the FWC must be protected for values of $KE_{eff} > 123$ J (91 ft—lbf). The large mass of a FWC is also a hazard because of the potential for an accident when a FWC is being moved. In such an accident, the effective kinetic energy could easily exceed 123 J (91 ft—lbf) by orders of magnitude. The large mass is a hazard even when a FWC is at rest. If a FWC lay on a hard protuberance such as one of the indenters in this investigation, the FWC could be damaged and the tension strength seriously reduced. Thus, great care must be taken when a FWC is placed in a cradle or rigged for moving.

Appendix

The term n_0 in Hertz's equation is defined as[13]

$$n_0 = \frac{4}{3}(k_1 + k_2)^{-1} \qquad (A1)$$

where

$$k_1 = (1 - \nu_1^2)\, E_1^{-1}$$

$$k_2 = \frac{1}{2} A_{22}^{1/2} \{[(A_{11}A_{22})^{1/2} + G_{zr}]^2 - (A_{12} + G_{zr})^2\}^{1/2} G_{zr}^{-1/2} (A_{11}A_{22} - A_{12}^2)^{-1}$$

and

$$A_{11} = E_z [1 - 2\nu_{rz}^2 E_z E_r^{-1} (1 - \nu_r)^{-1}]^{-1}$$

$$A_{22} = A_{11} (E_r E_z^{-1} - \nu_{rz}^2)(1 - \nu_r^2)^{-1}$$

$$A_{12} = A_{11} \nu_{rz} (1 - \nu_r)^{-1}$$

The E_1 and ν_1 are the elastic constants of the isotropic sphere and the E_r, E_z, G_{zr} ν_r, and ν_{rz}, are the elastic constants of the transversely isotropic semi—infinite body in polar coordinates.

References

(1) Loyd, B. A.; and Knight, G. K.: Impact Damage Sensitivity of Filament-Wound Composite Pressure Vessels. 1986 JANNAF Propulsion Meeting, CPIA Publication 455 Vol. 1, August 1986, pp. 7-15.

(2) Poe, C. C., Jr.; Illg, W.; and Garber, D. P.: A Program to Determine the Effect of Low-velocity Impacts on the Strength of the Filament-wound Rocket Motor Case for the Space Shuttle. NASA TM-87588, September 1985.

(3) Poe, C. C., Jr.; Illg, W.; and Garber, D. P.: Hidden Impact Damage in Thick Composites. Proceedings of the Review of Progress in Quantitative Nondestructive Evaluation, Vol. 5B, pp. 1215-1225, 1986.

(4) Poe, C. C., Jr.; Illg, W.; and Garber, D. P.: Tension Strength of a Thick Graphite/epoxy Laminate after Impact by a 1/2-In.-Radius Impacter. NASA TM-87771, July 1986.

(5) Poe, C. C., Jr.; and Illg, W.: "Strength of a Thick Graphite/Epoxy Rocket Motor Case After Impact by a Blunt Object," Test Methods for Design Allowables for Fibrous Composites, ASTM STP 1003, C. C. Chamis, Ed., American Society for Testing and Materials, Philadelphia, 1989. pp. 150-179. (Also in NASA TM-89099, February 1987 and in 1987 JANNAF Composite Motor Case Subcommittee Meeting, CPIA Publication 460, Feb. 1987, pp. 179-202.)

(6) Poe, C. C., Jr.: Surface Crack Analysis Applied to Impact Damage in a Thick Graphite/Epoxy Composite. Surface Crack Growth: Models, Experiments and Structures, ASTM STP 1060, W. G. Reuter, J. H. Underwood, and J. C. Newman, Jr., Eds., American Society for Testing and Materials, Philadelphia, 1990, pp. 194-212. (Also in NASA TM-100600, April 1988.)

(7) Harris, C., E.; and Morris, D. H.: Preliminary Report on Tests of Tensile Specimens with a Part-Through Surface Notch for a Filament-Wound Graphite/Epoxy Material. NASA CR-172545, 1985.

(8) Madaras, E. I.; Poe, C. C., Jr.; Illg, W.; and Heyman, J. S.: Estimating Residual Strength in Filament Wound Casings from Non-Destructive Evaluation of Impact Damage. Proceedings of the Review of Progress in Quantitative Nondestructive Evaluation, Vol. 6B, pp. 1221-1230, 1986.

(9) Madaras, E. I.; Poe, C. C., Jr.; and Heyman, J. S.: Combining Fracture Mechanics and Ultrasonics NDE to Predict the Strength Remaining in Thick Composites Subjected to Low-Level Impact. 1986 Ultrasonics Symposium Proceedings, Ed. B. R. McAvoy, New York, Institute of Electrical and Electronic Engineers. Vol. 86CH2375-4, No. 2, pp. 1051-1059.

(10) Madaras, E. I.; Poe, C. C., Jr.; and Heyman, J. S.: A Nondestructive Technique for Predicting the Strength Remaining in Filament Wound Composites Subjected to Low-Level Impact. 1987 JANNAF Composite Motor Case Subcommittee Meeting, CPIA Publication 460, Feb. 1987, pp. 249-258.

(11) Poe, C. C., Jr.: Simulated Impact Damage in a Thick Graphite/Epoxy Laminate Using Spherical Indenters. Proceedings of American Society for Composites. November 1988. (Also in NASA TM-100539, January 1988.)

(12) Poe, C. C., Jr.: Relevance of Impacter Shape to Nonvisible Damage and Residual Tensile Strength of a Thick Graphite/Epoxy Laminate. NASA TM-102599, April 1990.

(13) Greszczuk, Longin B.: Damage in Composite

Materials due to Low Velocity Impact. Impact Dynamics, John Wiley & Sons, Inc., 1982, pp. 55-94.
(14) Chatterjee, Sailendra N.: Surface Cracks in Thick Laminated Fiber Composite Plates. Surface Crack Growth: Models, Experiments and Structures, ASTM STP 1060, W. G. Reuter, J. H. Underwood, and J. C. Newman, Jr., Eds., American Society for Testing and Materials, Philadelphia, 1990, pp. 177-193.
(15) Love, A. E. H.: The Stress Produced in a Semi-infinite Solid by Pressure on Part of the Boundary. Phil. Trans. Roy. Soc. Lond. Series A, Vol. 228, 1929, pp. 377-420.
(16) Newman, J. C., Jr.; and Raju, I. S.: Stress-Intensity Factor Equations for Cracks in Three-Dimensional Finite Bodies. Fracture Mechanics: Fourteenth Symposium—Volume I: Theory and Analysis, ASTM STP 791, American Society for Testing and Materials, 1983, pp. I-238-I-268.